Experimental Demonstration of Germanium-on-Silicon Slot Waveguides at Mid-Infrared Wavelength

Jinha Lim, Joonsup Shim, Dae-Myeong Geum, and Sanghyeon Kim, *Member, IEEE*

***Abstract*—We first demonstrated a slot waveguide based on a Ge-on-Si (GOS) platform with a 3 μm thickness of the Ge in the mid-infrared wavelength range at 4.2 μm. We numerically designed the slot waveguide to have a large field confinement in the slot for sensing application. Based on the design, we fabricated the GOS slot waveguide with a slot gap of 200 nm, which is coupled with in-out grating couplers. We characterized the propagation loss of the waveguides by the cut-back method and carefully compared it with channel waveguides. In fundamental TE mode, the propagation loss in the channel waveguide and the slot waveguide were quite similar (5.20 and 4.86 dB/cm, respectively), whereas the field confinement was much higher in the slot waveguides. Additionally, we simulated and analyzed the loss of the devices in terms of radiation, sidewall roughness scattering, material absorption by free-carrier absorption (FCA), and CO_2. These results strongly suggest that the fabricated slot waveguide based on the GOS platform would be one of the promising building blocks for the optical gas sensor platform.**

***Index Terms*—Slot waveguides, mid-infrared, Ge-on-Si, confinement factor, propagation loss.**

I. Introduction

THE mid-infrared (MIR) wavelength range, from 2 to 20 μm, has been of significant interest for many applications such as environmental monitoring [1], biochemical sensing [2], optical communication [3], and spectral imaging [4]. In particular, unique absorption lines of the chemicals and biomolecules enable spectroscopy and sensing in this MIR range. The absorption characteristics due to the vibrational transition of their atomic bonds are exhibited in the so-called MIR "fingerprint" region. Also, the MIR region has atmospheric transmission windows of 3–5 μm and 8–13 μm that are crucial for the applications.

Manuscript received January 13, 2022; revised March 31, 2022; accepted April 11, 2022. Date of publication April 19, 2022; date of current version May 12, 2022. This work was supported in part by the National Research Foundation of Korea under Grant 2020R1F1A1052718, in part by Alchemist Project under Grant 20012263, in part by Atmospheric Environment Research Program funded by KIST Institutional Program under Grant 2E31372, and in part by BK21 FOUR. *(Corresponding author: Sanghyeon Kim.)*

The authors are with the School of Electrical Engineering, Korea Advanced Institute of Science and Technology, Daejeon 34141, South Korea (e-mail: ljh9105@kaist.ac.kr; shimjs@kaist.ac.kr; gdmgdm@kaist.ac.kr; shkim.ee@kaist.ac.kr).

Digital Object Identifier 10.1109/JPHOT.2022.3167695

However, a conventional sensing system in the MIR has the limitations of large volumes, cost, and high power consumption. To overcome these constraints, an on-chip sensor based on photonic integrated circuits (PICs) is strongly needed in terms of cost-effectiveness as well as device scaling. In near-infrared (NIR), Si photonics with Si-on-insulator (SOI) is a successful technology for highly compact devices in optical interconnection and optical sensing applications through mature fabrication technologies high compatibility with complementary metal-oxide-semiconductor (CMOS), good optical confinement thanks to low material losses in NIR, and high refractive index contrast. However, this platform is not appropriate in the broad MIR due to material absorption. In order to expand the availability of Si photonics technology to the MIR region, low-loss Si-based SOIs were used [5], [6]. Additionally, to avoid the narrow spectral coverage of the buried oxide (BOX) layer of SiO_2, which has a strong absorption band up to approximately 4 μm [7], [8], Si-on-nitride (SON) [9], Si-on-sapphire (SOS) [10], Si-on-calcium-fluoride (SOCF) [11], and Si-on-lithium-niobate (SOLN) [12] have been investigated for MIR photonics integration, but the limitation of not covering all MIR region still remains.

Considering a suitable platform, Ge is the best candidate for photonic devices in group-IV materials, since it is transparent over a wide MIR region (∼15 μm) and is fully CMOS compatible. Recently, PICs based on the Ge material have been extensively proposed with various forms such as Ge-on-Si (GOS) [13], [14], Ge-on-insulator (GOI) [15], [16], Ge-on-nitride (GON) [14], Ge-on-SOI [17], and SiGe-on-Si [18]. Among these, the GOS platform attracts a lot of interest for providing a useful MIR wavelength range and ease of the process for fabrication. Since the technology of strain engineering in epitaxial growth and high-speed operation of devices with digital/analog in advanced CMOS process has emerged, the GOS platform has been explored for active devices [19], [20], as well as passive circuits. Meanwhile, to build up the detecting part on a chip-scale, an on-chip thermal detector using TiO_x/Ti/TiO_x bolometric thin-film on GOI platforms has been proposed lately [21]. Moreover, on-chip integrated MIR light sources such as interband cascade lasers (ICLs) [22] and quantum cascade lasers (QCLs) [23], have been already demonstrated. By combining these detectors and sources with the passive devices in a single chip, it is possible to implement on-chip sensors with GOS

in MIR sensing applications. Notably, it is well known that Ge CMOS transistors can show higher performances than Si transistors due to high carrier mobilities [24]. Additionally, the developing technology of monolithic 3D (M3D) integration on Ge [25], [26] can provide versatile functionalities such as digital, analog, MEMS, sensors, and displays. Therefore, Ge-based PIC has a great potential to be a new platform for MIR optical sensors.

To facilitate the Ge-based PIC consisting of several parts of active and passive components, all components should be required. Among them, passive devices play a key role in guiding light in the core and forming evanescent field adjacent surroundings. Especially, maximizing the confinement of the evanescent field in the external region is critical to enhancing the interaction with the absorptive environment. Meanwhile, suspended Ge platforms were reported [27], [28] to reduce the optical loss. These results provide good optical confinement and low propagation loss. However, slot-guided structures also have the advantages of performance as good as the suspended structures with a relatively easy fabrication process. Thus, to improve the performance of the sensor, the slot structure [29] carrying high optical confinement in a very narrow gap with a low index would be an excellent candidate. The slot waveguide, which is comprised of two core rails of a high-index material with the sub-wavelength gap of a low-index region can well confine high optical intensity by using the electric field discontinuity due to index-contrast at the interface between the rails and slot. It leads to enhancement of the light-matter interaction. Actually, biochemical sensors [30]–[32], electro-optic (EO) modulators [33]–[35], and light-emitting devices [36], [37] based on the slot waveguides showed superior performances to channel waveguide in the NIR range. With these superior performances, however, there is no trial to implement the slot waveguides working at the MIR range for Ge-based optical sensors. Exploiting the slot structure based on the GOS platform can lead to enhancement of the light-matter interaction in the MIR range and improvement of the sensitivity for the sensor.

Therefore, in this paper, we first proposed and evaluated the slot-guided waveguide on the GOS platform for the optical sensor at the MIR region. To enhance optical interaction with the cladding region rather than the core, we designed and optimized the geometry of the slot waveguide to higher confinement factor Γ, which represents the ratio of the confined field in the air and slot as an important figure-of-merit for the optical sensor. Then, we fabricated the GOS channel and slot waveguides. Additionally, evaluation of the propagation properties in this platform was successfully conducted by using optical measurement at 4.2 μm in the fundamental TE mode. Based on these results, we also analyzed the loss mechanism for the GOS waveguide by the simulation.

II. Designs of GOS Waveguides for MIR

We designed two types of GOS waveguides, including channel and slot waveguides. The schematic of structures with the channel and the slot waveguides are shown in Fig. 1(a) and (b), where W, H, G, and h_{slab} are the width, height, gap of the slot, and slab height under the slot in the waveguide, respectively. In

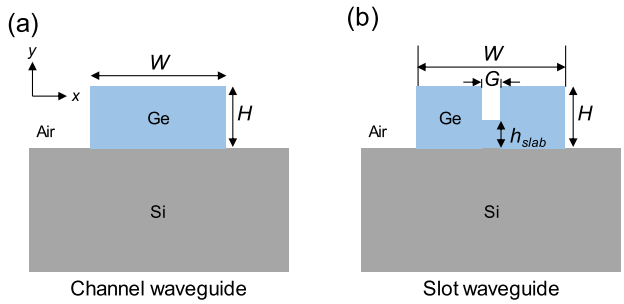

Fig. 1. Schematic cross-section of (a) channel and (b) slot waveguides of Ge-on-Si (GOS). W, H, G, and h_{slab} are the width, height, gap, and slab height of the core. G is the gap separated by two rails in the slot. In the case of the slot, core width W is the sum of the width of two rails and the gap.

the slot waveguide, it is clear that quasi-TE mode is significantly more sensitive to external medium refractive index changes than quasi-TM mode [38]. Thus, the surroundings of the sensor in the TE mode of the waveguide interact with a stronger evanescent field than the TM mode.

Γ is a crucial parameter of light-matter interactions in the external region (air and slot) of the waveguide for the optical sensor and the expression is defined as [2].

$$\Gamma = \frac{n_g}{\mathrm{Re}(n_{\mathrm{clad}})} \frac{\int\int_{\mathrm{clad}} \varepsilon_{\mathrm{clad}} |\boldsymbol{E}|^2 dxdy}{\int\int_{\infty}^{+\infty} \varepsilon |\boldsymbol{E}|^2 dxdy} \times 100\% \tag{1}$$

where n_{g}, n_{clad}, and $\varepsilon_{\mathrm{clad}}$ are the group velocity, refractive index and relative permittivity of the cladding, respectively, and $\boldsymbol{E}$ represents the electric fields vector. Γ is proportional to a ratio of the cross-sectional integrals of electromagnetic fields in the xy-plane of the cladding region and the total region in the xy-plane. The characteristics such as the electromagnetic field components and the group velocities of the GOS waveguides were simulated using the eigenmode solver. (MODE, Ansys Lumerical) The waveguides were optimized to be fabricated on GOS wafers with a thick Ge layer of 3 μm on Si to avoid leaky-wave in the substrate region.

Fig. 2(a) and (b) show the calculated Γ, which is simulated in the quasi-TE and -TM, respectively, in the air region according to (1) for channel waveguides with different W of a 3 μm thickness of GOS. Similarly, Fig. 2(c) and (d) represent Γ for the TE and TM of the slot waveguides as a function of W and G. h_{slab} was assumed to be 1 μm considering our fabrication tolerance of dry etching in a single step. Of course, the slot waveguides with fully etched slabs would exhibit much higher Γ due to the widened slot gap for the field confinement. Nevertheless, Γ of the slot waveguides with the nonzero slab thickness considering our fabrication constraint still is greater than the channel waveguides at the peak values for the TE polarization. Moreover, the TE (x-polarized) shows much stronger field confinement in the air region rather than the TM (y-polarized). The TE mode in the channel waveguide is guided when W is larger than 1.05 μm. Also, Γ is reduced due to the field being strongly localized in the core with the 3-μm thickness, as the core width becomes wide. In the case of the TE mode, Γ of the slot waveguide (17.1%, $W = 2.05/G = 0.1$ μm) is greater than the channel waveguide

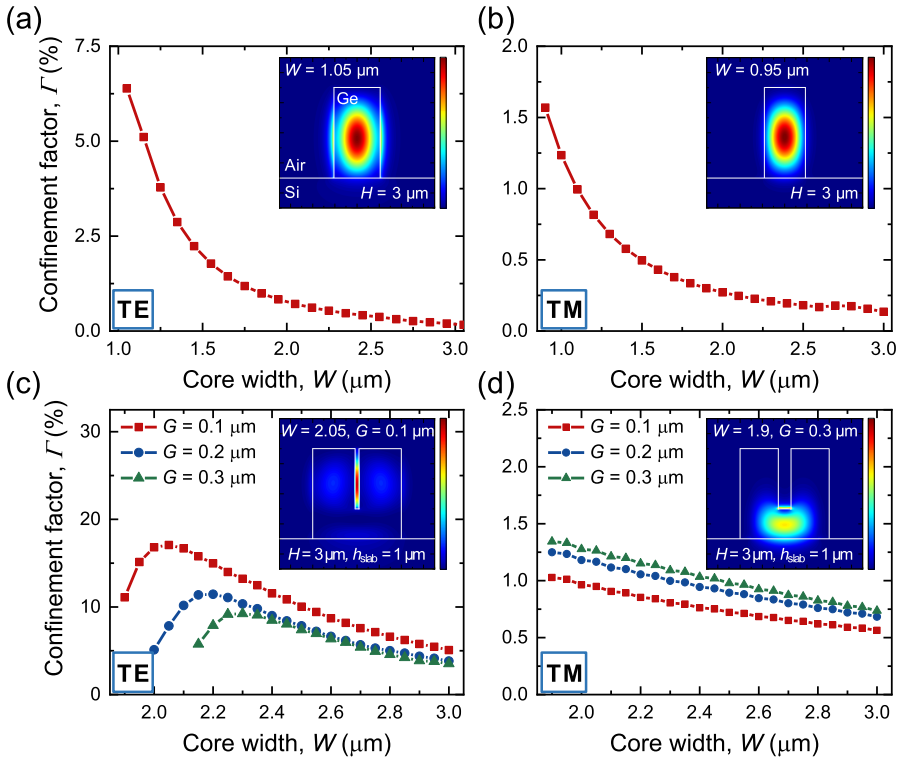

Fig. 2. Confinement factor Γ as a function of W of the channel waveguides where H and h_{slab} are 3 μm and 1 μm, respectively, for (a) TE and (b) TM. Similarly, Γ of the slot waveguides for (c) TE and (d) TM. Each inset in the graph shows the normalized field distribution and at the specific dimensions, which have a peak intensity of Γ.

(6.39%, $W = 1.05$) at peak values of each geometric condition. With an increase in the size of the waveguide core, the ratio of the evanescent field in the cladding, which is consists of the slot and air, decreases owing to the increase of the portion of the modal field in the core. In the case of the slot waveguide where G is 0.1 μm, the electromagnetic wave starts to guide through the slot region with W roughly larger than 2 μm. Naturally, a larger G needs a larger W for guiding the electromagnetic wave. Similar to the channel waveguides, Γ decreases as an increase of W. However, the smaller size of these geometric conditions leads to the significant enhancement of confinement in the quasi-TE mode. Therefore, the higher field confinement in the slot waveguide was achieved in the narrower G.

III. Fabrication and Experiment Setup

Based on our numerical design for optimized Γ for the GOS waveguides and grating couplers to guide the TE mode, the fabrication for the GOS devices was carried out. The waveguides and grating couplers were fabricated with a 3 μm thick Ge core layer grown on a silicon substrate. Since the sufficiently thick core of the waveguide could avoid radiation loss to the substrate, we employed the structure. Fig. 3 shows the fabrication process flow of the GOS device. Initially, the GOSs were cleaned with acetone, methanol, and deionized (DI) water. After the cleaning, the native oxide of Ge was removed by a diluted 1:6 HF and DI for 30 seconds. Then, we deposited 20 nm-thick SiO_2 by the RF sputter system as a buffer layer, which is used to prevent the

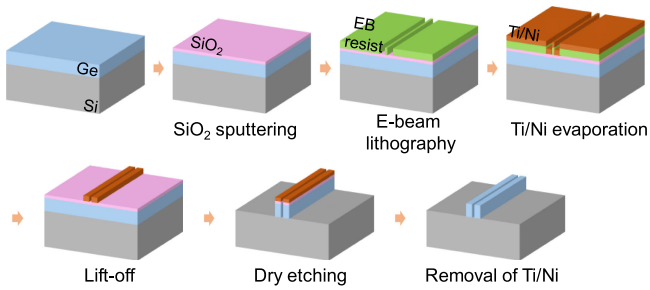

Fig. 3. Schematic of the fabrication process flow of the GOS slot waveguide by using electron-beam lithography and a lift-off method.

upper layer from contacting directly on GOS. In order to define a nanoscale size of G and a precise width of the waveguide, electron-beam lithography (EBL) was used. Furthermore, to minimize the line edge roughness of the electron-beam (EB) resist of poly (methyl methacrylate) (PMMA) for smooth sidewall roughness, we optimized the dose condition in the EBL process. After the formation of the PMMA, the metal layers of Ti (2 nm) and Ni (200 nm) were deposited by electron-beam evaporation. To enhance adhesion, an extremely thin adhesion layer of Ti was applied between SiO_2 and Ni layers. Subsequently, to etch the Ge layer for formation of the core, an inductively coupled plasma reactive ion etch (ICP-RIE, Oxford) process in chlorine (10 sccm) and argon (30 sccm) at a 150 W RF power and 1000 W ICP power in 10 mTorr vacuum pressure was carried out. Then, the core and slot were etched down with the depth of 2 μm and

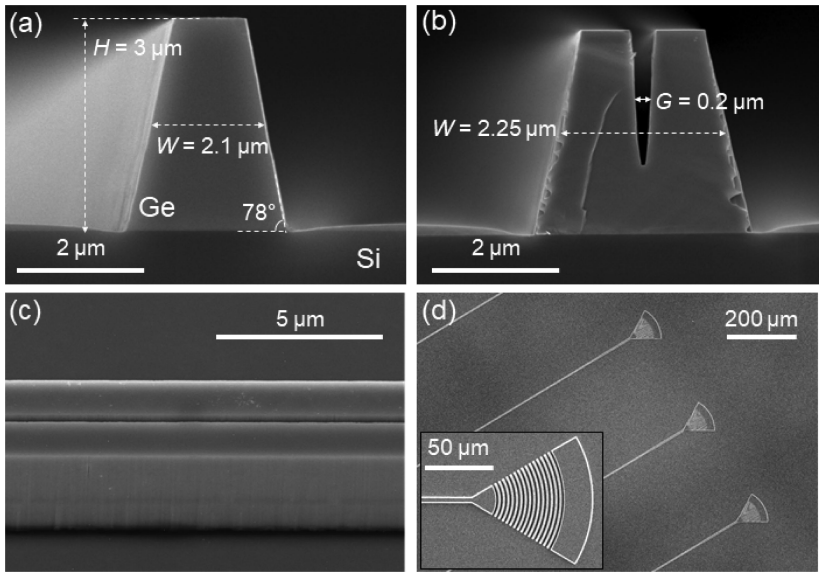

Fig. 4. SEM image of the GOS waveguide with the 3-μm thickness of Ge core. Cross-sectional image of the core in (a) channel, (b) slot waveguide. (c) Observation for the sidewall roughness of the slot waveguide. (d) Top-view of a focusing grating coupler.

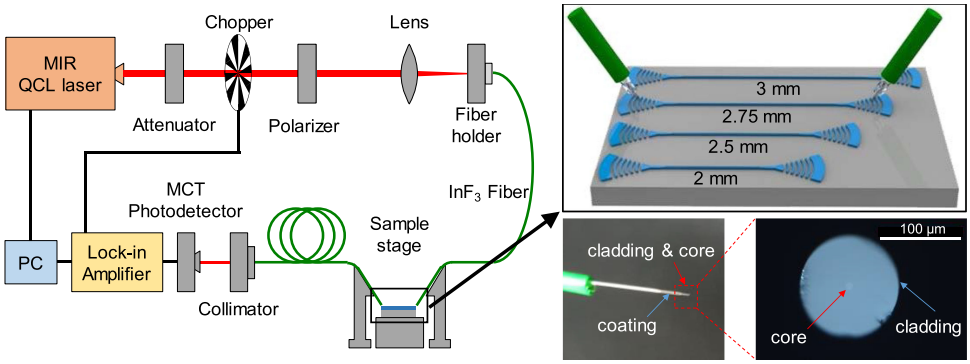

Fig. 5. Experimental setup for measuring the propagation loss of waveguides using MIR QCL laser of 4.2 μm wavelength, MCT photodetector, and elaborately cleaved InF_3 fiber. 4 different lengths of the waveguide are 2.25, 2.5, 2.75, and 3 mm. Each waveguide has grating couplers to couple the light with InF_3 optical fibers.

3 μm, respectively due to the ICP-RIE lag effect. Finally, the mask of Ti/Ni was removed by a diluted 1:6 of HCl and DI, and SiO_2 was etched by the HF solution.

Fig. 4(a) and (b) show cross-sectional scanning electron microscope (SEM) images of fabricated the 3 μm of GOS channel and slot waveguide, respectively, showing clear geometry of channel and slot. The dimension of each channel and slot waveguide was fabricated to have a different width that exhibits the optimum confinement factor. For a deeply etched slot in the single step with a nanoscale gap, 200 nm of G is defined with 2.25 and 2.5 μm of W for the slot waveguide. To minimize the scattering loss due to the sidewall roughness, the dry etching condition and dose of EB resist have been optimized, thereby, the smooth sidewall surface was achieved as shown in Fig. 4(c) regardless of the configurations. Fig. 4(d) shows the SEM image of the focusing grating coupler, which we designed and optimized to couple the light of the fundamental TE mode into the waveguide and out to the free-space for a 4.2 μm wavelength. The grating coupler, which has a period of 3.2 μm and an etch depth of 3 μm with a duty cycle of 0.22 was designed by using the 3D finite-difference time-domain (FDTD, Ansys lumerical) method considering the wavelength, numerical aperture, beam diameter, and incidence angle of the light for our optical fibers. The calculated coupling efficiency of the grating coupler shows 41.5%.

The propagation loss of the waveguides was characterized using the cut-back method, which measures the transmission through waveguides with known differential lengths as described in Fig. 5. The 4.2 μm laser with a QCL (Daylight Solution MIRcat) in free-space is modulated using a chopper (Scitec instruments, 300CD) with 1 kHz before coupling into an indium fluoride (InF_3) fiber (Thorlabs). The sophisticated facet of the InF_3 fiber was obtained using a fiber cleaver (FK11, Photonics Kinetics) for the achievement of high coupling efficiency between the fiber and the grating coupler as shown in the inset of Fig. 5. The collimated beam of the laser was focused on the launch end of the InF_3 fiber using an aspheric lens. The TE-polarized MIR light, which is coupled out of the fiber is

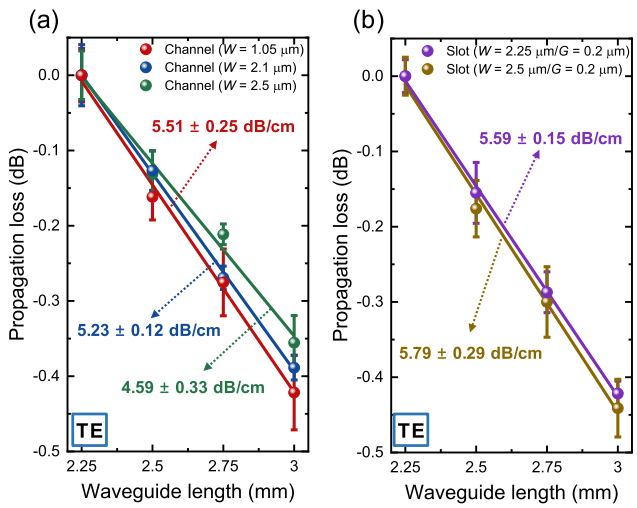

Fig. 6. Propagation loss measurement for TE polarization at 4.2 μm. (a) The core widths of the channel waveguides are 1.05, 2.1, and 2.5 μm (b) The core widths of the slot waveguides are 2.25, and 2.5 μm when G is 0.2 μm.

coupled into/out from the GOS waveguide via the focusing grating couplers, then the light propagates to a cooled mercury cadmium telluride (MCT) photodetector (Thorlabs), which is used to measure the transmission of the MIR light, then a lock-in amplifier (Stanford Research, SR-850) was used to enhance the signal-to-noise ratio (SNR) of the output. In this experiment, we measured four different lengths of the waveguides with 2.25, 2.5, 2.75, and 3 mm for both channel and slot waveguides as shown in the inset of Fig. 5.

IV. Measurement Results

Using the measurement setup with the MIR optical fiber, we measured the propagation loss for the fabricated channel and slot waveguides guiding the TE mode via the optimized grating coupler for the TE polarization. We evaluated the three different sizes of the channel waveguides ($W = 1.05$, 2.1, and 2.5 μm), and two different sizes of the slot waveguide ($W = 2.25$, and 2.5 μm) when G is 0.2 μm at a fixed wavelength of 4.2 μm for the quasi-TE polarization. Waveguide losses of the TE mode in the range of 4.59–5.51 dB/cm for the channel waveguide and 5.59–5.79 dB/cm for the slot waveguide were measured as shown in Fig. 6(a) and (b), respectively. The propagation loss of the channel and slot waveguides were measured by 5 times for transmission power of each length of the waveguide and the values for the transmission were averaged. The averaged losses are indicated with the circles in the graph, and the standard deviations are marked with the error bars. Additionally, the solid lines are linear fitting to the averaged data. In all configurations of the waveguide, the propagation loss is more significant as the core width is decreased due to the leakage toward the substrate that is caused by lower confinement in the core. Additionally, material loss by free-carrier absorption (FCA) and carbon dioxide (CO_2) at 4.2 μm wavelength can affect the loss characteristic in the waveguide. Therefore, we further discuss the loss mechanisms in the next paragraph.

It is well known that the propagation loss in the waveguide is an essential parameter to evaluate the system of communication and the sensor. Therefore, we analyzed the measured propagation loss by numerically exploring the loss factors caused by geometrical effects and material properties of the GOS waveguides. Particularly, the propagation loss dominantly depends on radiation, sidewall roughness, FCA in the material, and background absorption. Considering these four types of the loss, the total propagation loss coefficient can be expressed as

$$\alpha_{\text{total}} = \alpha_{\text{radiation}} + \alpha_{\text{scattering}} + \alpha_{\text{FCA}} + \alpha_{\text{background}} \tag{2}$$

where $\alpha_{\text{radiation}}$ is the radiative loss due to leakage toward the substrate, $\alpha_{\text{scattering}}$ is the scattering loss caused by sidewall roughness, α_{FCA} is the material absorption by FCA in both core and substrate, and $\alpha_{\text{background}}$ is the loss of the external environment of the device. To investigate the loss influenced by the mechanisms, we simulated each type of loss as shown in Fig. 7. Except above loss mechanisms, further factors, which affect the guiding loss in the waveguide are being as described in [39], such as defects at the interface of the epitaxial layer, native oxide on the surface, "time-dependent haze" formation interstitial oxygen or carbon, and multiphonon absorption.

First, the radiative loss as a function of the core width due to coupling toward the substrate with the height of 3 μm is shown in Fig. 7(a) at 4.2 μm. These calculated losses of the channel and slot waveguide are 0.023 dB/cm and 0.114 dB/cm, as the core widths are 1.05 μm and 2.1 μm, respectively, where Γ is maximum. Becoming larger than a certain size of the core width, regardless of the configuration, the radiation loss is nearly saturated dB/cm of 10^{-4} level, because most of the electric field is confined in the core or two rails. Especially for the slot waveguide, however, the propagation loss is more significant as the W is decreased due to the leakage toward the substrate that is caused by lower confinement in the core despite the thick Ge. In order to suppress the radiation loss, sufficiently high isolation of the core structure from the substrate by a BOX layer should be explored.

Second, scattering loss by sidewall roughness is needed to be taken into consideration, since the sidewall roughness of the waveguide is caused inevitably by an inductively coupled plasma reactive ion etch (ICP-RIE) in the fabrication step. Especially, in NIR wavelength, a numerical investigation of scattering loss with SOI optical waveguide had already been reported [40], because it is important to analyze the influence of the surface roughness in a waveguide with a relatively small size compared to the dimension of the MIR waveguide. According to the equation of Rayleigh scattering, which is the relation of inversely proportional to λ^4 for scattering cross-section, fortunately, the loss by surface roughness is negligible. Also, analytical calculations for the scattering loss coefficient in dB scale can be written as

$$\alpha_{\text{scattering}} = 4.34 \frac{\sigma^2}{k_0 \sqrt{2} d^4 n_{\text{core}}} g(v) f(x) \tag{3}$$

The perturbed sidewall surface is described by the root mean square (rms) deviation σ as roughness from the flatness of

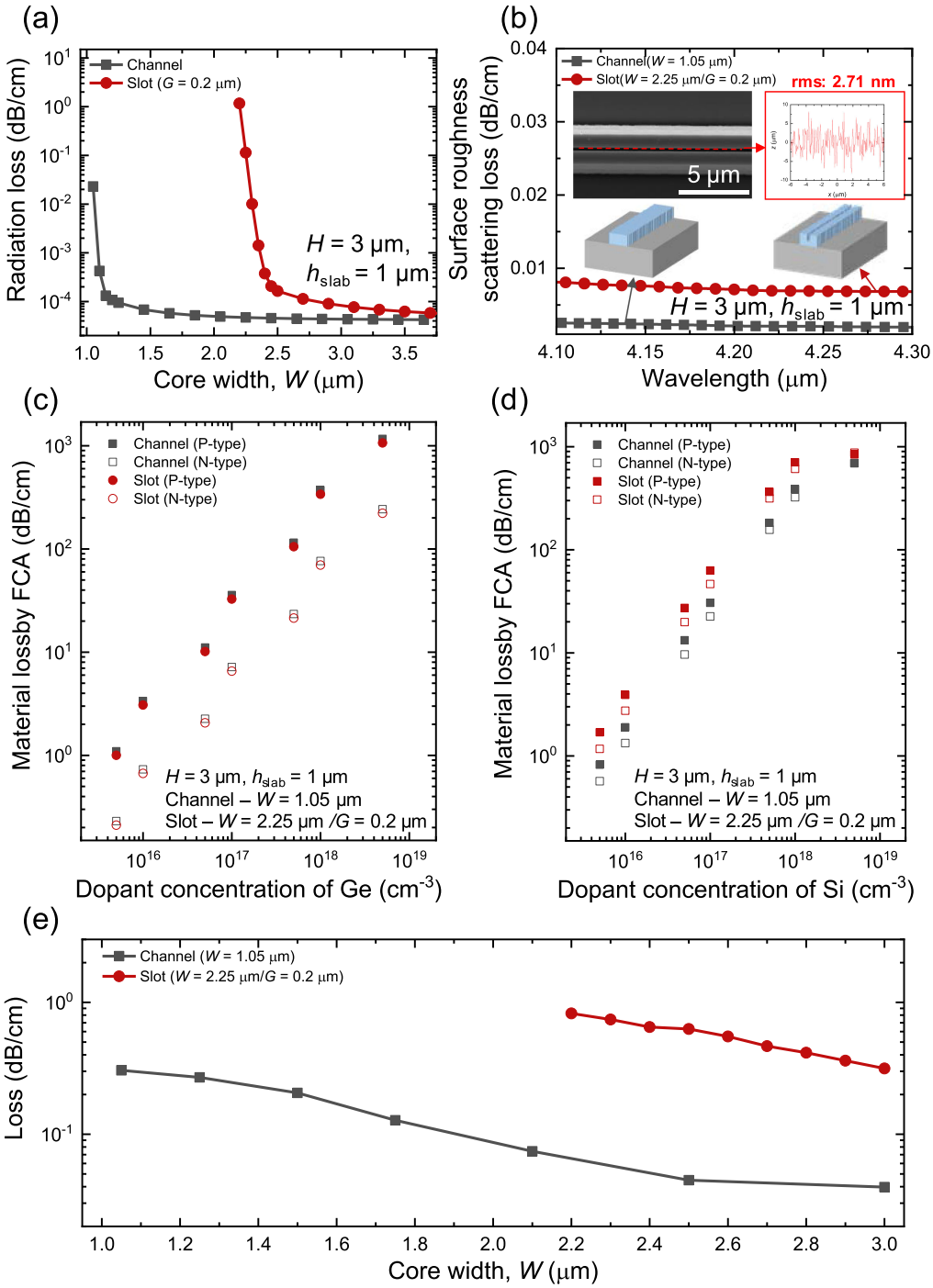

Fig. 7. Investigation for four types of mechanisms in the propagation loss by (a) radiation toward to the substrate, (b) scattering due to the sidewall roughness (inset; rms roughness, and simulated structures), material loss by FCA for (c) Ge and (d) Si as a function of dopant concentration, and (e) background (CO_2) absorption.

the waveguide. This relation is derived from the Gaussian autocorrelation function with standard deviation linked to the roughness parameter σ, a function related to waveguide geometry $g(v)$ and sidewall roughness $f(x)$, where d is the half-width of the core, n_{core} is the refractive index of the core, the geometry $g(v) = u^2v^2/(1+w)$, and the function $f(x) = x[1-x^2+\{(1+x^2)^2+2x^2\gamma^2\}^{1/2}]^{1/2}/\{(1+x^2)^2+2x^2\gamma^2\}^{1/2}$. u, v, w, x, and γ are defined in [40]. Using this relation, the analytic result of sidewall roughness scattering in the fundamental TE mode of GOS waveguides for wavelengths up to 9.0 μm is shown [39]. To verify this, the scattering loss except for any other components of the loss is simulated by the 3D FDTD, as shown in Fig. 7(b). We estimated the sidewall roughness of the waveguide as the rms values of 2.71 nm by extracting the profile of the waveguide's sidewall, as shown in the inset of the images and graph. Then, we generated grains randomly with the rms roughness at all

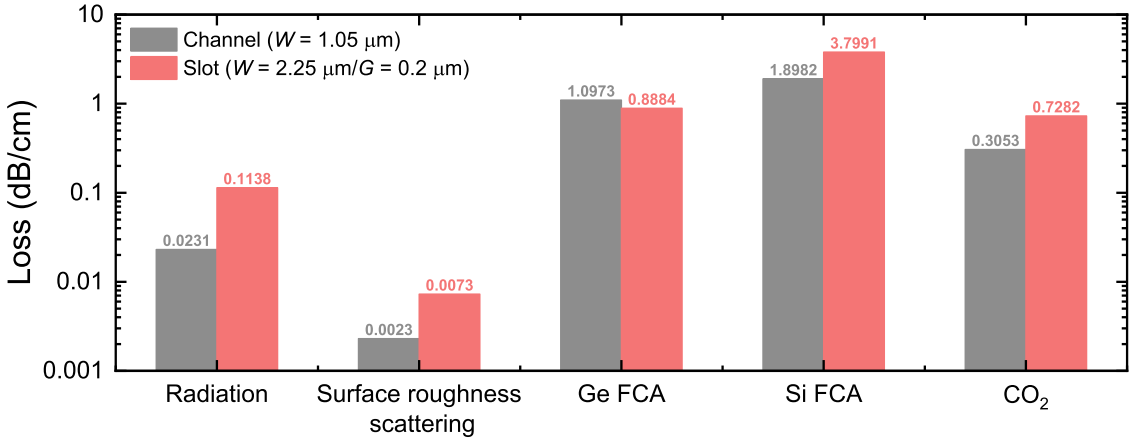

Fig. 8. Investigation of the loss mechanism including material, radiation, scattering, and background (CO_2) loss for the fabricated channel ($W = 1.05$ μm) and slot waveguide ($W = 2.25$ μm/$G = 0.2$ μm).

sidewalls of the waveguide in the FDTD, as depicted in the inset structures. The scattering losses, which are 0.0023 dB/cm and 0.0073 dB/cm of the channel and slot, respectively, are less significant than the radiative loss in the optimum dimensions.

Generally, it would be enough to consider the propagation loss with just radiation and scattering in the guiding mode. However, in the case of the doped semiconductor, material loss is also quite critical for the propagation loss in the waveguide. Using the absorption coefficient by FCA of the material for the core and substrate with various doping concentrations in both p- and n-type [42], [43], we calculated the additional loss of the waveguides by FCA as a function of the doping concentration of Ge and Si at 4.2 μm wavelength as shown in Fig. 7(c) and (d), respectively. Here, we assumed that the other materials in each case do not show any absorption thereby, α_{FCA} in the waveguide is caused by the only core or substrate. In the lossy Ge core, the loss of the channel waveguide is slightly larger than the slot waveguide due to the large portion of guiding light in the core of the channel waveguide. However, considering that the only substrate is lossy, the material loss of the slot waveguide is larger than the channel waveguide owing to the behavior of high radiative loss in the slot waveguide. In the same doping concentration, the absorption coefficient of p-type material is greater than n-type.

Finally, the waveguides should undergo the background absorption $\alpha_{\mathrm{background}}$, which affects the propagation loss due to the overlapped mode field with the external region. Unfortunately, the module of our QCL cannot avoid the CO_2 absorption spectra. Furthermore, the measurement was conducted in a normal atmosphere including CO_2. Nevertheless, the 4.2 μm wavelength for our module of the QCL has low CO_2 absorption, which is at a tail of CO_2 spectra. Using the HITRAN CO_2 absorption coefficient (2.9434 cm^{-1}) in the normal atmosphere (300 K, 1 atm.) [44], the waveguide loss caused by the CO_2 background was calculated as shown in Fig. 7(e). The propagation losses of CO_2 absorption for the channel ($W = 1.05$ μm) and slot ($W = 2.25$, $G = 0.2$ μm) waveguide are 0.305 dB/cm and 0.728 dB/cm, respectively. Due to the slot waveguide having higher confinement than the channel waveguide, $\alpha_{\mathrm{background}}$ of the slot waveguide is greater. It is certain that $\alpha_{\mathrm{background}}$ is proportional to Γ.

To investigate the loss mechanism for the measured samples rigorously, we estimated all four types of practical losses based on the simulation. For both fabricated channel (W = 1.05 μm) and slot waveguide (W = 2.25 μm/G = 0.2 μm), 1) radiative loss, 2) surface roughness scattering loss, 3) FCA loss, and 4) background loss are shown in Fig. 8. Though it is provided that the radiation and the scattering have less impact on the propagation loss, the material losses of the GOS waveguide by FCA could lead to considerable propagation loss, due to the high doping concentration of Si substrate and Ge core being around 10^{16} cm^{-3} of p-type. Particularly, among these losses, the substrate loss has a much more degrading effect on the performance as 1.898 dB/cm for the channel and 3.791 dB/cm for the slot waveguide. According to the loss simulation, which shows greater radiative loss of the slot waveguide than the channel waveguide, the optical loss of the slot waveguide can be more affected by the lossy substrate. In this experiment, overlapping the material loss by as much as radiation leaking to the substrate, the propagation loss is increased, which further deteriorates performance. Although these results were higher than the high- quality of Ge waveguides [45], [46], the loss characteristics can be further improved by using a low-loss material and measuring in the vacuum. As assuming the environment is vacuum by excluding the CO_2 absorption for each device, especially, the losses could be 4.55–5.2 dB/cm and 4.86–5.16 dB/cm for the channel and slot waveguide, respectively. Therefore, the propagation loss will be improved to 5.2 dB/cm for the channel ($W = 1.05$ μm) and 4.86 dB/cm for the slot waveguide ($W = 2.25/G = 0.2$ μm).

As mentioned above, the angled sidewall, as well as etch depth, were not perfect due to the fabrication tolerance. The achieved etch angle of the sidewall is 78°. Practically, Γ of the fabricated channel and slot when G is 0.2 μm is calculated as shown in Fig. 9. W is a lateral size at the center of the height of the Ge core. The difference of Γ between the steep-sloped sidewall and the angled sidewall for the channel ($W = 1.05$ μm) and the slot ($W = 2.25$ μm) are 4.63% and 1.52%, respectively. In the channel waveguides, the mode of the field is formed in

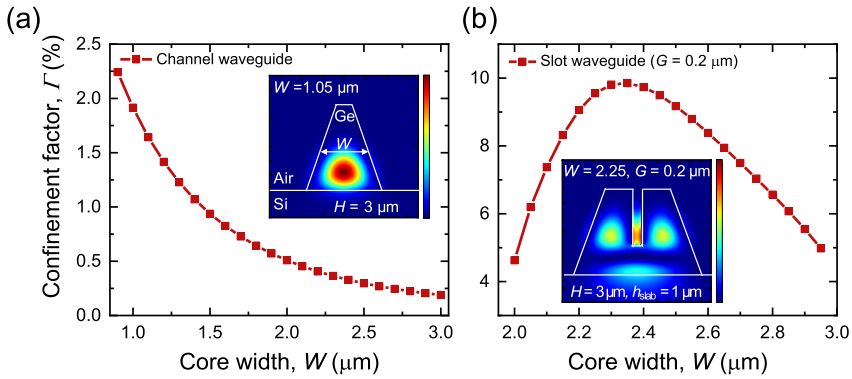

Fig. 9. Γ as a function of W of (a) the fabricated channel and (b) slot waveguide considering the angled sidewalls. The sidewall angle of the waveguide is 78°.

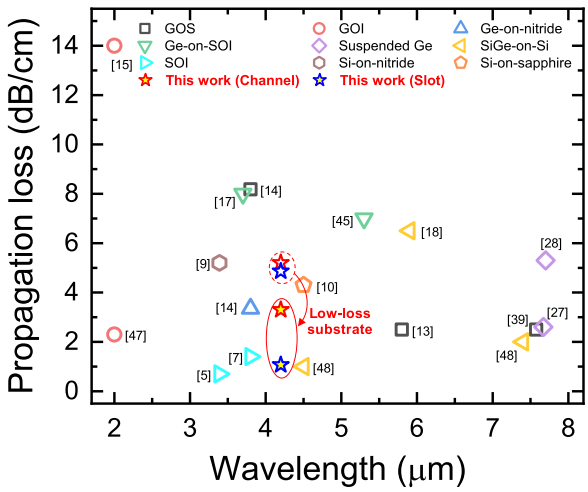

Fig. 10. The benchmark plot of propagation loss at the MIR range for the waveguides based on various platforms: GOS, GOI, Ge-on-nitride, Ge-on-SOI, suspended Ge, SiGe-on-Si, SOI, Si-on-nitride, and Si-on-sapphire.

the lower part of the core that is relatively wider than the upper part and confined well in the core. Thus, it is smaller than the steep sidewall waveguide. Similarly, in the slot waveguides, it is slightly decreased compared to the proposed structure owing to the light partially guiding under the slot. In other words, the evanescent field outside the core with the angled sidewall was confined less than the waveguide with the steeped sidewall. However, that effect becomes weak in the slot waveguide due to the high field being confined in the slot. This fabrication tolerance can be improved by using CF_4-based dry etching, which will provide steep sidewalls as we initially designed.

Fig. 10 shows the benchmark for the propagation loss of various photonic platforms such as GOS, GOI, Ge-on-SiN_x, Ge-on-SOI, suspended Ge, SiGe-on-Si, SOI, Si-on-nitride, and Si-on-sapphire at the MIR range. Our GOS waveguides demonstrated in this work show moderate propagation losses, but they will be definitely improved to 3.3 dB/cm for the channel waveguide, and 1.07 dB/cm for the slot waveguide by changing the substrate and even lower with GOI structure, which can provide better light confinement. Therefore, we believe that the slot waveguide can be used for the optical gas sensor in the MIR range owing to its high confinement factor and low propagation loss.

V. Conclusion

In summary, we first demonstrated the slot waveguide based on a GOS platform for the optical sensors at the MIR and analyzed the performance of the device with numerical simulation and experiment. The slot waveguide was superior to the channel waveguide in terms of Γ because of the large difference in the refractive indices between the core of the Ge waveguide and G with the low-index material. Although the fabricated devices have a sloped sidewall with 78°, Γ of the slot waveguide is superior to the channel waveguide. Therefore, we successfully demonstrated the Ge slot waveguide with the propagation loss of 4.86–5.16 dB/cm on GOS photonic platforms.

References

[1] P. D. LeVan and Ü. Sakoglu, "Infrared sensing technologies assisting environmental monitoring," in *Proc. Infrared Sensors, Devices, Appl. X*, 2020, pp. 38–49.
[2] M. Vlk *et al.*, "Extraordinary evanescent field confinement waveguide sensor for mid-infrared trace gas spectroscopy," *Light Sci. Appl.*, vol. 10, no. 1, 2021, Art. no. 26 doi: 10.1038/s41377-021-00470-4.
[3] J. J. Liu, B. L. Stann, K. K. Klett, P. S. Cho, and P. M. Pellegrino, "Mid and long-wave infrared free-space optical communication," in *Proc. Laser Commun. Propag. through Atmos. Oceans VIII*, 2019, Art. no. 1113302.
[4] M. H. Köhler *et al.*, "Hyperspectral imager for the mid-infrared spectral range using a single-mirror interferometer and a windowing method," *OSA Continuum*, vol. 2, no. 11, pp. 3212–3222, 2019, doi: 10.1364/osac.2.003212.
[5] G. Z. Mashanovich *et al.*, "Low loss silicon waveguides for the mid-infrared," *Opt. Exp.*, vol. 19, no. 8, pp. 7112–7119, 2011, doi: 10.1364/OE.19.007112.
[6] S. A. Miller *et al.*, "Low-loss silicon platform for broadband mid-infrared photonics," *Optica*, vol. 4, no. 7, pp. 707–712, 2017, doi: 10.1364/optica.4.000707.
[7] J. S. Penadés, A. Z. Khokhar, M. Nedeljkovic, and G. Z. Mashanovich, "Low-loss mid-infrared SOI slot waveguides," *IEEE Photon. Technol. Lett.*, vol. 27, no. 11, pp. 1197–1199, Jun. 2015.
[8] R. Soref, "Mid-infrared photonics in silicon and germanium," *Nat. Photon.*, vol. 4, no. 8, pp. 495–497, 2010, doi: 10.1038/nphoton.2010.171.
[9] S. Khan, J. Chiles, J. Ma, and S. Fathpour, "Silicon-on-nitride waveguides for mid- and near-infrared integrated photonics," *Appl. Phys. Lett.*, vol. 102, no. 12, 2013, Art. no. 121104, doi: 10.1063/1.4798557.
[10] T. Baehr-Jones *et al.*, "Silicon-on-sapphire integrated waveguides for the mid-infrared," *Opt. Exp.*, vol. 18, no. 12, pp. 12127–12135, 2010, doi: 10.1364/OE.18.012127.
[11] B. Kumari, R. K. Varshney, and B. P. Pal, "Design of a silicon-on-calcium-fluoride-based compact and efficient polarization rotator for

the mid-IR," *OSA Continuum*, vol. 1, no. 4, pp. 1158–1171, 2018, doi: 10.1364/osac.1.001158.
[12] J. Chiles and S. Fathpour, "Mid-infrared integrated waveguide modulators based on silicon-on-lithium-niobate photonics," *Optica*, vol. 1, no. 5, pp. 350–355, 2014, doi: 10.1364/optica.1.000350.
[13] Y.-C. Chang *et al.*, "Low-loss germanium strip waveguides on silicon for the mid-infrared," *Opt. Lett.*, vol. 37, no. 14, pp. 2883–2885, 2012, doi: org/10.1364/OL.37.002883.
[14] W. Li *et al.*, "Germanium-on-silicon nitride waveguides for mid-infrared integrated photonics," *Appl. Phys. Lett.*, vol. 109, no. 24, 2016, Art. no. 241101, doi: 10.1063/1.4972183.
[15] J. Kang, M. Takenaka, and S. Takagi, "Novel Ge waveguide platform on Ge-on-insulator wafer for mid-infrared photonic integrated circuits," *Opt. Exp.*, vol. 24, no. 11, 2016, Art. no. 11855, doi: 10.1364/oe.24.011855.
[16] S. Kim, J.-H. Han, J.-P. Shim, H.-J. Kim, and W. J. Choi, "Verification of Ge-on-insulator structure for a mid-infrared photonics platform," *Opt. Mater. Exp.*, vol. 8, no. 2, pp. 440–451, 2018, doi: 10.1364/ome.8.000440.
[17] A. Malik *et al.*, "Ge-on-Si and Ge-on-SOI thermo-optic phase shifters for the mid-infrared," *Opt. Exp.*, vol. 22, no. 23, pp. 28479–28488, 2014, doi: 10.1364/OE.22.028479.
[18] Q. Liu, "Mid-infrared sensing between 5.2 and 6.6 μm wavelengths using Ge-rich sige waveguides," *Opt. Mater. Exp*, vol. 8, no. 5, pp. 1305–1312, 2018.
[19] J. Michel, J. Liu, and L. C. Kimerling, "High-performance Ge-on-Si photodetectors," *Nat. Photon.*, vol. 4, no. 8, pp. 527–534, 2010, doi: 10.1038/nphoton.2010.157.
[20] J. Cui and Z. Zhou, "High-performance Ge-on-Si photodetector with optimized DBR location," *Opt. Lett.*, vol. 42, no. 24, pp. 5141–5144, 2017, doi: 10.1364/OL.42.005141.
[21] J. Shim, J. Lim, D.-M. Geum, B. H. Kim, S.-Y. Ahn, and S. Kim, "Tailoring bolometric properties of a TiOx/Ti/TiOx tri-layer film for integrated optical gas sensors," *Opt. Exp.*, vol. 29, no. 12, pp. 18037–18058, 2021, doi: 10.1364/OE.427147.
[22] H. Lotfi *et al.*, "Monolithically integrated mid-IR interband cascade laser and photodetector operating at room temperature," *Appl. Phys. Lett.*, vol. 109, no. 15, 2016, Art. no. 151111, doi: 10.1063/1.4964837.
[23] A. Spott *et al.*, "Quantum cascade laser on silicon," *Optica*, vol. 3, no. 5, pp. 545–551, 2016, doi: 10.1364/optica.3.000545.
[24] H.-R. Lim *et al.*, "Impact of bottom-gate biasing on implant-free junctionless Ge-on-insulator n-MOSFETs," *IEEE Electron Device Lett.*, vol. 40, no. 9, pp. 1362–1365, Sep. 2019, doi: 10.1109/led.2019.2931410.
[25] S.-H. Kim *et al.*, "Heterogeneous integration toward a monolithic 3-D chip enabled by III–V and Ge materials," *IEEE J. Electron Devices Soc.*, vol. 6, pp. 579–587, 2018, doi: 10.1109/jeds.2018.2802840.
[26] D.-M. Geum *et al.*, "Monolithic 3D integration of InGaAs photodetectors on SI MOSFETs using sequential fabrication process," *IEEE Electron Device Lett.*, vol. 41, no. 3, pp. 433–436, Mar. 2020, doi: 10.1109/led.2020.2966986.
[27] A. Osman *et al.*, "Suspended low-loss germanium waveguides for the longwave infrared," *Opt. Lett.*, vol. 43, no. 24, pp. 5997–6000, 2018, doi: 10.1364/OL.43.005997.
[28] A. Sánchez-Postigo *et al.*, "Suspended germanium waveguides with subwavelength-grating metamaterial cladding for the mid-infrared band," *Opt. Exp.*, vol. 29, no. 11, pp. 16867–16878, 2021, doi: 10.1364/OE.422764.
[29] V. R. Almeida, Q. Xu, C. A. Barrios, and M. Lipson, "Guiding and confining light in void nanostructure," *Opt. Lett.*, vol. 29, no. 11, pp. 1209–1211, 2004, doi: 10.1364/ol.29.001209.
[30] C. A. Barrios *et al.*, "Slot-waveguide biochemical sensor," *Opt. Lett.*, vol. 32, no. 21, pp. 3080–3082, 2007, doi: 10.1364/ol.32.003080.
[31] L. Singh Sulabh, S. Jain, and M. Kumar, "Optical slot waveguide with grating-loaded cladding of silicon and titanium dioxide for label-free bio-sensing," *IEEE Sens. J.*, vol. 19, no. 15, pp. 6126–6133, Aug. 2019, doi: 10.1109/jsen.2019.2910278.
[32] Q. Liu *et al.*, "Highly sensitive Mach–Zehnder interferometer biosensor based on silicon nitride slot waveguide," *Sens. Actuators B Chem.*, vol. 188, pp. 681–688, 2013, doi: 10.1016/j.snb.2013.07.053.
[33] Z. Lu and W. Zhao, "Nanoscale electro-optic modulators based on graphene-slot waveguides," *J. Opt. Soc. Amer. B*, vol. 29, no. 6, pp. 1490–1496, 2012, doi: 10.1364/josab.29.001490.
[34] F. Qiu *et al.*, "A hybrid electro-optic polymer and TiO_2 double-slot waveguide modulator," *Sci. Rep.*, vol. 5, no. 1, 2015, Art. no. 8561, doi: 10.1038/srep08561.
[35] R. Palmer *et al.*, "High-speed, low drive-voltage silicon-organic hybrid modulator based on a binary-chromophore electro-optic material," *J. Lightw. Technol.*, vol. 32, no. 16, pp. 2726–2734, Aug. 2014, doi: 10.1109/jlt.2014.2321498.
[36] A. Tengattini *et al.*, "Toward a 1.54 μm electrically driven erbium-doped silicon slot waveguide and optical amplifier," *J. Lightw. Technol.*, vol. 31, no. 3, pp. 391–397, Feb. 2013.
[37] F. Vogelbacher *et al.*, "Slot-waveguide silicon nitride organic hybrid distributed feedback laser," *Sci. Rep.*, vol. 9, no. 1, 2019, Art. no. 18438, doi: 10.1038/s41598-019-54655-4.
[38] F. Dell'Olio and V. M. Passaro, "Optical sensing by optimized silicon slot waveguides," *Opt. Exp.*, vol. 15, no. 8, pp. 4977–4993, 2007, doi: 10.1364/oe.15.004977.
[39] M. Nedeljkovic *et al.*, "Germanium-on-silicon waveguides operating at mid-infrared wavelengths up to 8.5 μm," *Opt. Exp.*, vol. 25, no. 22, pp. 27431–27441, 2017.
[40] F. Grillot, L. Viv, S. Laval, and E. Cassan, "Propagation loss in single-mode ultrasmall square silicon-on-insulator optical waveguides," *J. Lightw. Technol.*, vol. 24, no. 2, pp. 891–896, Feb. 2006, doi: 10.1109/jlt.2005.861939.
[41] F. P. Payne and J. P. R. Lacey, "A theoretical analysis of scattering loss from planar optical waveguides," *Opt. Quantum Electron.*, vol. 26, no. 10, pp. 977–986, 1994, doi: 10.1007/bf00708339.
[42] M. Nedeljkovic, R. Soref, and G. Z. Mashanovich, "Predictions of free-carrier electroabsorption and electrorefraction in germanium," *IEEE Photon. J.*, vol. 7, no. 3, Jun. 2015, Art no. 2600214, doi: 10.1109/jphot.2015.2419217.
[43] M. Nedeljkovic, R. Soref, and G. Z. Mashanovich, "Free-carrier electrorefraction and electroabsorption modulation predictions for silicon over the 1-14 μm infrared wavelength range," *IEEE Photon. J.*, vol. 3, no. 6, pp. 1171–1180, Dec. 2011.
[44] E. Pannier, "Radis–The radiation software," *Github.*io. Accessed: Jan. 11, 2022. [Online]. Available: http://radis.github.io
[45] U. Younis, S. K. Vanga, A. E.-J. Lim, P. G.-Q. Lo, A. A. Bettiol, and K.-W. Ang, "Germanium-on-SOI waveguides for mid-infrared wavelengths," *Opt. Exp.*, vol. 24, no. 11, pp. 11987–11993, 2016, doi: 10.1364/oe.24.011987.
[46] J. Kang *et al.*, "Focusing subwavelength grating coupler for mid-infrared suspended membrane germanium waveguides," *Opt. Lett.*, vol. 42, no. 11, pp. 2094–2097, 2017, doi: 10.1364/OL.42.00209.
[47] Z. Zhao *et al.*, "Low-loss Ge waveguide at the 2-μm band on an n-type Ge-on-insulator wafer," *Opt. Mater. Exp.*, vol. 11, no. 12, pp. 4097–4106, 2021, doi: 10.1364/OME.444071.
[48] M. Brun *et al.*, "Low loss sige graded index waveguides for mid-IR applications," *Opt. Exp.*, vol. 22, no. 1, pp. 508–518, 2014, doi: 10.1364/OE.22.000508.